SUPPLEMENT TO THE *WELDING JOURNAL*, SEPTEMBER 2018
Sponsored by the American Welding Society

Influence of Multiple Gleeble®-Simulated Weld Thermal Cycles on Maraging 17-4 and 13-8+Mo

A preliminary investigation to determine whether controlled weld metal deposition procedures are feasible for Maraging Stainless Steels 17-4 and 13-8+Mo

BY R. J. HAMLIN AND J. N. DuPONT

ABSTRACT

Multipass welding provides an opportunity to restore the strengthening precipitates that dissolve during primary welding thermal cycles by using the heat from subsequent weld passes. In the current investigation, a Gleeble® thermo-mechanical simulator was used to subject samples of 17-4 and 13-8+Mo to primary and secondary thermal cycles representative of 1000 and 2000 J/mm heat input multipass welds. Both the unaffected age-hardened base metal and as-deposited weld metal were considered to investigate the precipitation response of each. Hardness measurements were recorded after each thermal cycle to estimate the extent of precipitate dissolution or growth. The secondary welding thermal cycles were sufficient to promote hardening in both the base metal and weld metal for each heat input, indicating precipitate growth was occurring. Alloy 17-4 demonstrated a higher precipitation response when compared to 13-8+Mo that was attributed to an increased level of supersaturation and larger temperature range in which precipitation could occur. Additionally, the weld metal and base metal possessed similar precipitation responses for each material. Microchemical measurements and solidification simulations showed that backdiffusion relieves the concentration gradients in the weld that can form during solidification. These results explain the similarities in precipitation response between the base metal and weld metal. The results of this work demonstrate that controlled weld metal deposition may be used to eliminate the need for a postweld heat treatment (PWHT) in these alloys.

KEYWORDS

- Maraging Stainless Steels • Gleeble®
- Multipass Welding • Simulated Weld Thermal Cycles
- 17-4 • 13-8+Mo

Introduction

Martensitic precipitation-strengthened stainless steels 17-4 and 13-8+Mo possess a combination of high strength and relatively good ductility, making them ideal for applications in the military, aerospace, and nuclear industries (Refs. 1, 2). These alloys solidify as δ-ferrite and transform to austenite on cooling and martensite upon further cooling. Thus, the microstructure consists of a martensitic matrix with around 10–20% remnant δ-ferrite and less than a few percent retained austenite. The low percentage of retained austenite is due to the low carbon content in these systems (typically < 0.03 wt-%), which also results in a relatively ductile martensite and low carbide content. Therefore, changes in the mechanical properties of these alloys are largely controlled by the evolution of fine nanometer scale precipitates that form during heat treatment (Refs. 3, 4). Alloys 17-4 and 13-8+Mo are strengthened by BCC Cu precipitates and β-NiAl precipitates, respectively. When used in cast form, the alloys are homogenized to reverse microsegregation, solution treated and quenched to produce a supersaturated martensite, and then aged at temperatures between 450°C (842°F) and 620°C (1148°F) for times ranging from 1 to 5 hours to promote the formation of the strengthening precipitates (Refs. 3, 4). During the early stages of aging, the precipitates are on the order of 2–3 nm in size and highly coherent with the matrix, resulting in a significant increase in strength by forcing dislocation lines to shear through the particles. After prolonged aging, particle coarsening occurs that results in loss of coherency and causes dislocation lines to loop around the particles, concurrently decreasing the strength. If temperature is increased further, dissolution can occur, with an additional decrease in strength (Refs. 5, 6).

Large-scale applications involving these materials require joining with welding processes, which has provoked several studies on the effects of the welding thermal cycles on the properties of these alloys. The high temperatures experienced

https://doi.org/10.29391/2018.97.022

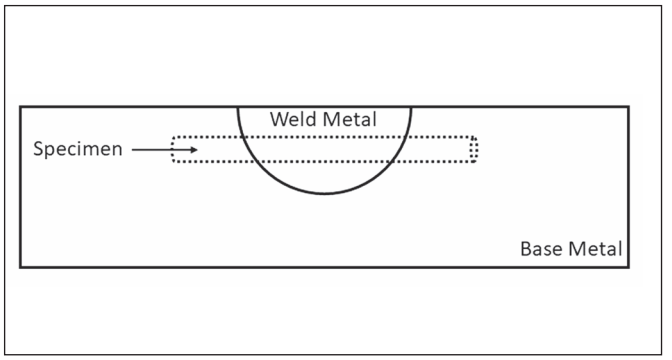

Fig. 1 — A schematic representing the cross section of the autogenous GTAW weld plates showing the location of Gleeble sample removal.

during welding are sufficient to result in microstructural changes such as martensite to austenite transformation, austenite to δ-ferrite transformation, and precipitate growth and dissolution (Refs. 7–9). Previous investigations on 17-4 and 13-8+Mo have demonstrated that the temperatures experienced in the heat-affected zone (HAZ) of fusion welds result in a significant decrease in strength that has been associated with precipitate dissolution (Ref. 7). Furthermore, it was demonstrated that the evolution of the matrix microstructural features such as martensite and δ-ferrite had minimal effect on the changes in properties. Instead, the changes in mechanical properties were the result of precipitate dissolution or growth (Ref. 7). Bhaduri et al. (Ref. 10) observed softening in the HAZ of 17-4 using hardness measurements and attributed the softening to the dissolution of precipitates. Although precipitate coarsening was considered, no direct evidence of coarsening was presented. In both experiments, it was observed that optimal properties could be achieved if a postweld heat treatment (PWHT) is applied. However, PWHTs are expensive and cannot be applied when welding on a large scale or making a repair in the field, necessitating development of optimized welding procedures that do not require PWHT.

Multipass welding provides an opportunity to reheat the region that softens during primary weld passes by the heat from secondary weld passes. Studies were performed by Yu et al. (Ref. 11) to investigate the effect of multiple welding thermal cycles on Cu precipitation in a low-carbon martensitic steel, BlastAlloy 160 (developed at Northwestern University). Atom probe tomography and hardness measurements demonstrated the precipitates dissolved during primary high-temperature thermal cycles and formed again during secondary thermal cycles representative of multipass welding (Ref. 11). If the times and temperatures associated with welding thermal cycles are sufficient to promote re-precipitation in 17-4 and 13-8+Mo, it may be possible to eliminate the need for PWHT by controlled weld metal deposition. The purpose of the current investigation is to determine the hardening response of these materials after exposure to primary and secondary thermal cycles representative of multipass welding. Two heat inputs were investigated as well as both age-hardened material and weld metal as starting conditions.

In the current investigation, peak aged material and weld metal were subjected to primary and secondary welding thermal cycles representative of multipass welding using a Gleeble® 3500 thermomechanical simulator. Hardness measurements were then used to estimate the extent of precipitate dissolution and growth. The precipitation response of the weld metal was investigated, in addition to the peak aged material, because the as-solidified microstructure differs significantly from the base metal. This difference in microstructure combined with the possible residual microsegregation from solidification may influence the precipitation response of the weld metal as compared to the heat-treated base metal. Brooks and Garrison (Ref. 1) determined by transmission electron microscopy (TEM) and mechanical testing that the weld metal of various precipitation-strengthened stainless steels, including 13-8+Mo, aged more rapidly at lower temperatures when compared to their respective base metals and were more resistant to overaging (coarsening) (Ref. 1). It was also observed in works by Bhaduri et al. (Ref. 10) that the hardening response of 17-4 weld metal was either faster or slower than the base metal depending on the base metal starting condition. Thus, it is important to consider the hardening response of the base metal and weld metal during exposure to multiple thermal cycles.

Another consideration when welding precipitation-strengthened alloys is the effect of heat input. Higher heat inputs will increase the temperature at greater distances into the base metal, thereby decreasing the thermal gradient

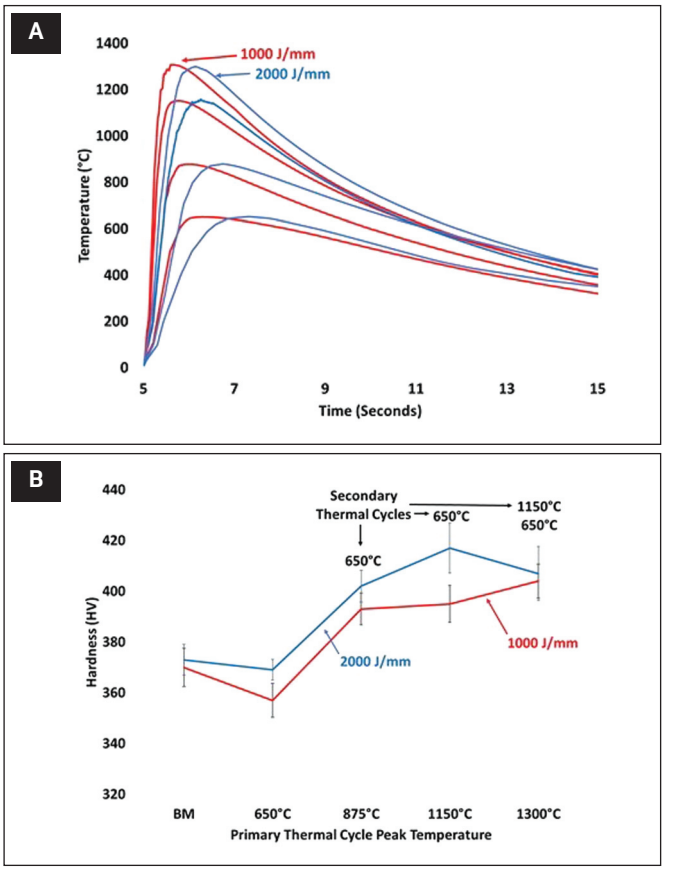

Fig. 2 — A — 1000 and 2000 J/mm thermal cycles used in the current investigation; B — hardness measurements recorded on 17-4 samples after exposure secondary thermal cycles shown in A.

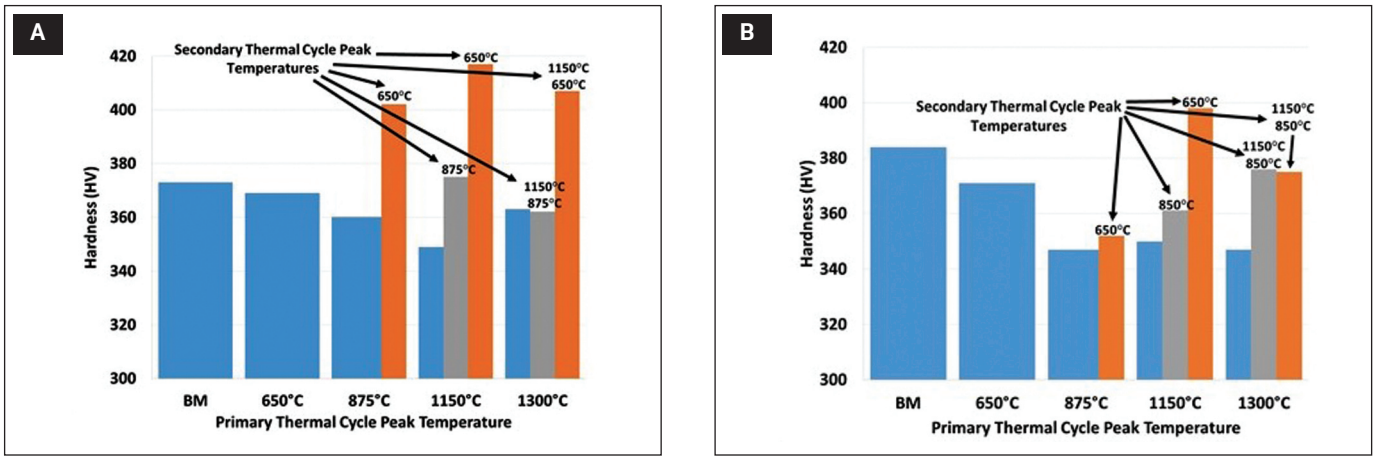

Fig. 3 — Hardness data for 2000 J/mm heat input Gleeble multipass welding simulations (blue bars indicate primary welding thermal cycles, orange and gray correlate to secondary welding thermal cycles): A — 17-4; B — 13-8+Mo.

and concurrently the cooling rate. Slower cooling rates will allow for more time at temperatures where growth can occur and may therefore provide additional strengthening during secondary thermal cycles. In the same work on 17-4 performed by Bhaduri et al. (Ref. 10), it was observed that the welding heat input had significant effects on both the hardness and tensile properties of weldments. However, it was also observed that a PWHT was still required to optimize properties (Ref. 10). Two heat inputs of 1000 and 2000 J/mm were used in the current investigation to simulate low and high heat inputs.

Experimental Procedure

The chemical compositions of 17-4 and 13-8+Mo used during this investigation can be seen in Table 1. Cast 17-4 and 13-8+Mo plates were hot isostatic pressed (HIPed) at 1162°C (2124°F) and 103 MPa (15 ksi) to eliminate porosity and minimize residual segregation from casting, and then air cooled to room temperature. The 17-4 and 13-8+Mo samples were solution treated at 1052°C (1926°F) and 926°C (1699°F), respectively. Following solution treatment, 17-4 samples were air cooled to room temperature and 13-8+Mo samples were argon gas cooled followed by a water quench to 15°C (59°F). Samples were then aged for 1.5 h at 579°C (1074°F) and 4 h at 593°C (1099°F) for 17-4 and 13-8+Mo, respectively. Autogenous gas tungsten arc (GTA) welds were made on a ½-in.-thick plate of each material using a current of 200 A, voltage of 10 V, travel speed of 1 mm/s, and 99.98% argon shielding gas.

Table 1 — Chemical Composition of PH 17-4 and PH 13-8+Mo Used in the Gleeble Simulated Multipass Welding Study (all values in wt-%)

	Fe	Cr	Ni	C	Mn	Cu	Mo	Al	Si	P	S	Nb
17-4	Bal.	16.08	4.09	0.03	0.41	3.02	0.21	0.00	0.83	0.03	0.01	0.20
13-8+Mo	Bal.	12.71	7.90	0.06	0.19	0.13	2.27	0.77	0.22	0.01	0.031	0.00

Table 2 — Weld Thermal Cycle Peak Temperature Combinations Used in This Study

Material	Primary Thermal Cycle Peak Temperature °C (°F)	Secondary Thermal Cycle Peak Temperature °C (°F)	Tertiary Thermal Cycle Peak Temperature °C (°F)
17-4	650 (1202)	X	X
17-4	875 (1607)	650 (1202)	X
17-4	1150 (2102)	650 (1202)	X
17-4	1150 (2102)	875 (1607)	X
17-4	1300 (2372)	1150 (2102)	650 (1202)
17-4	1300 (2372)	1150 (2102)	875 (1607)
13-8+Mo	650 (1202)	X	X
13-8+Mo	875 (1607)	650 (1202)	X
13-8+Mo	1150 (2102)	650 (1202)	X
13-8+Mo	1150 (2102)	850 (1562)	X
13-8+Mo	1300 (2372)	1150 (2102)	650 (1202)
13-8+Mo	1300 (2372)	1150 (2102)	850 (1562)

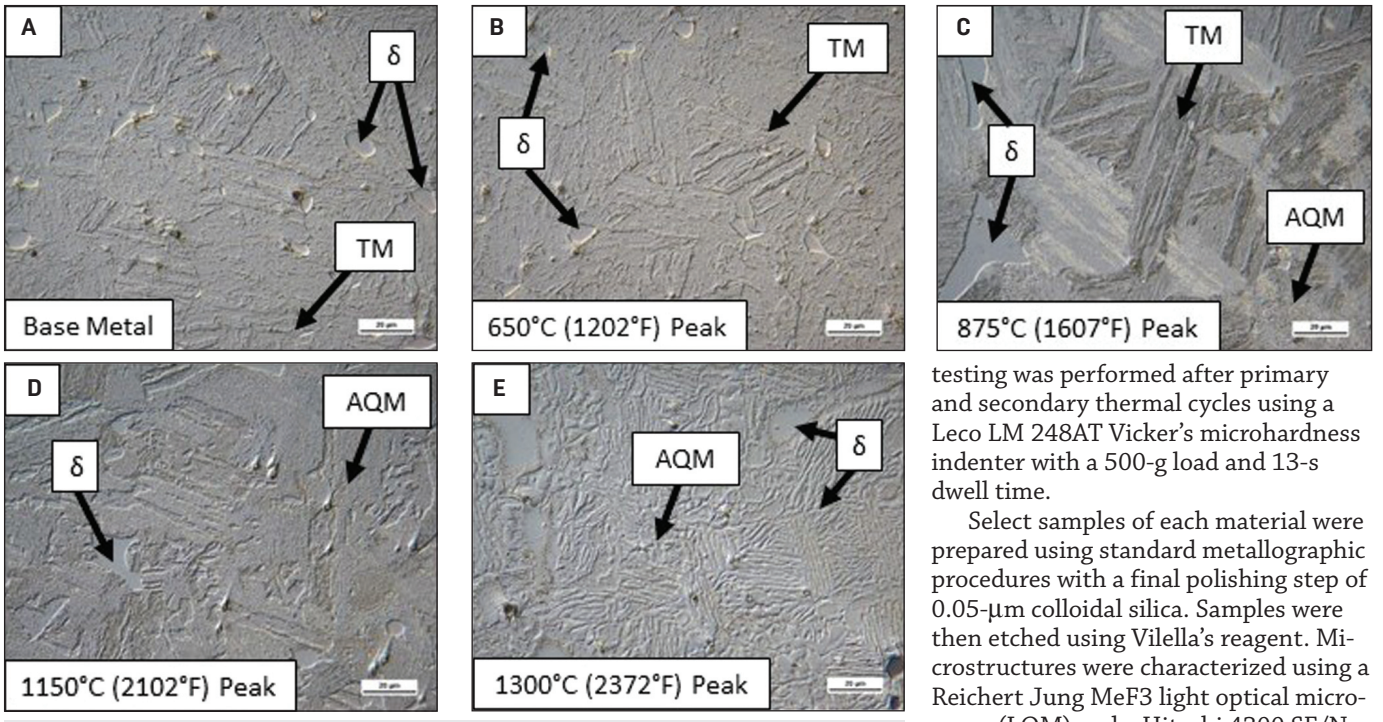

Fig. 4 — Light optical photomicrographs of 17-4: A — Base metal and after A; B — 650°C; C — 875°C; D — 1150°C; E — 1300°C thermal cycle. TM = tempered martensite, δ = delta ferrite, AQM = as-quenched martensite.

The aged plates were machined into 70-mm-long, 6-mm-diameter pins. Additional cross-weld samples of matching dimensions were machined from the GTA weld plates, with the weld metal centered in each pin as demonstrated in Fig. 1. A Gleeble® 3500 thermo-mechanical simulator was used to subject samples to various combinations of welding thermal cycles representative of multipass welding for a 1000 and a 2000 J/mm heat input. It should be noted that during the Gleeble experimentation, the cooling rates required for the 1000 J/mm thermal cycle could not be fully achieved, and therefore the data may not be entirely representative of a 1000 J/mm heat input.

However, the heating rates were achievable and the thermal cycles are still representative of a heat input lower than 2000 J/mm. This is demonstrated by the comparison in Fig. 2, showing thermal cycles and hardness measurements for both heat inputs for 17-4. Welding thermal cycles were calculated for four peak temperatures for each alloy using Sandia's SmartWeld program (Refs. 12, 13). Peak temperatures of 650°C (1202°F), 875°C (1607°F), 1150°C (2102°F), and 1300°C (2372°F) were used for 17-4 and 650°C (1202°F), 850°C (1562°F), 1150°C (2102°F), and 1300°C (2372°F) were used for 13-8+Mo. These four peak temperatures were chosen to represent the four major HAZ regions for each alloy based on recent work performed by Hamlin and DuPont (Ref. 7). Thermal cycle combinations are summarized in Table 2 and were chosen to simulate multipass welding. The region of a weld that is subjected to a high peak temperature primary thermal cycle may experience two additional thermal cycles during multipass welding depending on weld bead placement (Ref. 14). Thus, the 1300°C (2372°F) peak temperature has a tertiary thermal cycle as well. Hardness testing was performed after primary and secondary thermal cycles using a Leco LM 248AT Vicker's microhardness indenter with a 500-g load and 13-s dwell time.

Select samples of each material were prepared using standard metallographic procedures with a final polishing step of 0.05-µm colloidal silica. Samples were then etched using Vilella's reagent. Microstructures were characterized using a Reichert Jung MeF3 light optical microscope (LOM) and a Hitachi 4300 SE/N scanning electron microscope with an x-ray detector for energy-dispersive spectrometry (EDS). Microchemical measurements were performed across dendrites in weld metal samples by EDS. ThermoCalc thermodynamic modeling software was used in combination with the TCFE8 steels database to determine the solubility limits for precipitating elements in 17-4 and 13-8+Mo (Ref. 15).

Results and Discussion

Hardening Behavior and Evolution of Matrix Microstructures

Hardness data for the 17-4 and 13-8+Mo samples that were tested using a 2000 J/mm heat input can be seen in Fig. 3. After primary thermal cycles, the hardness decreased from 373 HV in the base metal to as low as 347 HV in the HAZ for 17-4, and from 384 HV in the base metal to as low as 347 HV in the HAZ for 13-8+Mo. Light optical photomicrographs of the base metal and the samples subjected to primary thermal cycles are shown in Figs. 4 and 5 for 17-4 and 13-8+Mo, respectively. As recently discussed in more detail, the microstructures consisted of varying amounts of tempered martensite, as-quenched martensite, and δ-ferrite (Ref. 7).

The austenite start and finish temperatures (Ac_1 and Ac_3) were recently measured via dilatometry to be 800°C (1472°F) and 925°C (1697°F) for Alloy 17-4 and 730°C (1346°F) and 900°C (1652°F) for Alloy 13-8+Mo (Ref. 7). The 650°C (1202°F) peak temperature thermal cycle did not reach Ac_1 and therefore the microstructure resembled the base metal for both alloys, with the exception of the martensite tempering that occurred. At 850°C (1562°F) for 13-8+Mo and 875°C (1607°F) for 17-4, the Ac_1 temperature was surpassed and partial transformation to austenite occurred on heating, resulting

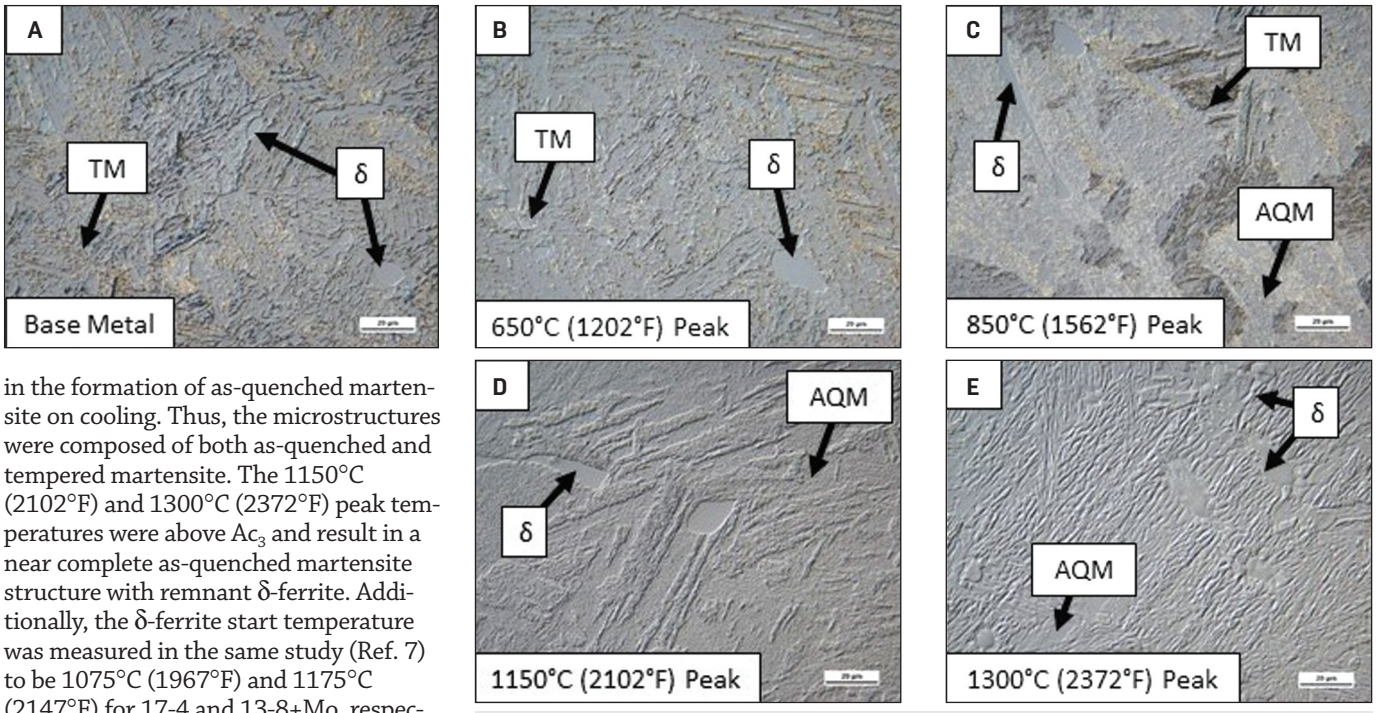

Fig. 5 — Light optical photomicrographs of 13-8+Mo: A — Base metal and after A; B — 650°C; C — 850°C; D — 1150°C; E — 1300°C thermal cycle. TM = tempered martensite, δ = delta ferrite, AQM = as-quenched martensite.

in the formation of as-quenched martensite on cooling. Thus, the microstructures were composed of both as-quenched and tempered martensite. The 1150°C (2102°F) and 1300°C (2372°F) peak temperatures were above Ac_3 and result in a near complete as-quenched martensite structure with remnant δ-ferrite. Additionally, the δ-ferrite start temperature was measured in the same study (Ref. 7) to be 1075°C (1967°F) and 1175°C (2147°F) for 17-4 and 13-8+Mo, respectively. This was evident from the microstructures for the 17-4 samples heated to 1150°C (2102°F) and 1300°C (2372°F) peak temperatures in which an increase in δ-ferrite along interlath locations was observed with increasing peak temperature. The same feature could be seen in the 13-8+Mo microstructure that was heated to 1300ºC (2372ºF).

The variations in the matrix microstructure discussed here do not account for the changes observed in hardness. The 1150°C (2102°F) and 1300°C (2372°F) peak temperature HAZ regions consisted primarily of as-quenched martensite, which was expected to be harder than the tempered martensite observed in the base metal and after a 650°C (1202°F) peak temperature thermal cycle (Refs. 3, 16). However, the hardness was higher in the tempered martensite regions when compared to the as-quenched martensite regions. Therefore, the variations in hardness were attributed to dissolution of the strengthening precipitates, rather than the changes to the matrix microstructures. Studies performed by Hochanadel et al. (Ref. 8) on the heat treatment of investment cast 13-8+Mo observed that, even after prolonged aging of 13-8+Mo, the β-NiAl precipitates remained small enough to suggest particles were not coarsening (Ref. 8). Other research performed by Ping et al. (Ref. 17) on β-NiAl and Bono et al. (Ref. 18) on Cu precipitation in similar systems found that segregation of elements such as Mo, Ni, and Mn to the precipitate/matrix boundary created a diffusion barrier that prevented precipitate coarsening. These findings, coupled with the decrease in hardness observed in the current investigation, suggest that precipitate dissolution was the primary mechanism active in these systems that caused reduced hardness. This was further supported by the hardness increase to near base metal levels or higher after exposure to secondary thermal cycles — Fig. 3. Such a large increase in hardness could only be due to precipitate growth. If the particles had coarsened after the primary thermal cycles, then reheating from secondary thermal cycles would only coarsen the particles further and a decrease in hardness would be expected (Refs. 5, 6). These results demonstrate that the precipitates dissolve during primary thermal cycles and significant re-precipitation and associated hardening can be achieved using secondary thermal cycles for a 2000 J/mm heat input. No secondary thermal cycles were used for the primary thermal cycle of 650°C (1202°F). This thermal cycle represents a subcritical peak temperature that is located on the edge of the HAZ and was therefore unlikely to experience significant reheating due to secondary weld passes (Ref. 14).

The hardness data for the 17-4 and 13-8+Mo samples that were subjected to thermal cycles representative of 1000 J/mm heat input can be seen in Fig. 6. A similar decrease in hardness was observed after primary thermal cycles along with a similar rise in hardness after application of the secondary thermal cycles. However, a smaller increase in hardness was observed for the subcritical secondary thermal cycles when compared to the results for the 2000 J/mm heat input. This trend was attributed to the decreased time available for precipitation at elevated temperature associated with the lower heat input thermal cycles.

Comparison of Precipitation Response between Base Metals

For both heat inputs, it was observed that the hardening response was slower in 13-8+Mo when compared to 17-4. This is demonstrated by the hardness comparison between 17-4 and 13-8+Mo for the 1000 J/mm shown in Fig. 7. Precipitate growth rates are controlled by two major factors, the

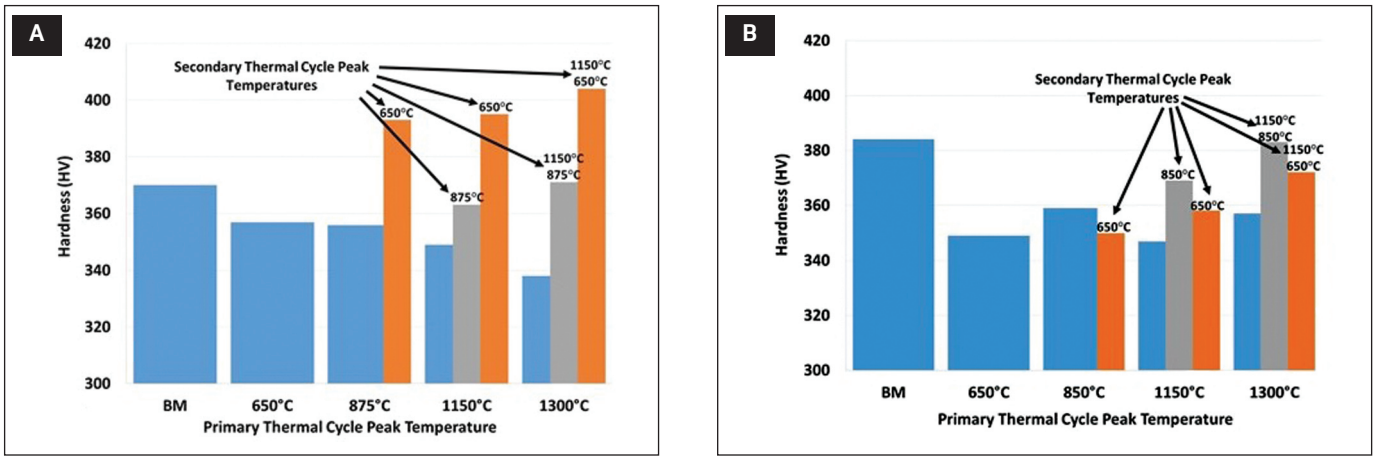

Fig. 6 — Hardness data for 1000 J/mm heat input Gleeble multipass welding simulations (blue bars indicate primary welding thermal cycles, orange and gray correlate to secondary welding thermal cycles): A — 17-4; B — 13-8+Mo.

diffusion rate of the precipitate solute element in the matrix and the supersaturation of these elements, which is the driving force for precipitate growth (Refs. 19, 20). Activation energies for diffusion of Cu, Al, and Ni in ferrite are 284, 235, and 245 kJ/mol, respectively, which would imply that precipitation may occur more rapidly in 13-8+Mo (that relies on the formation of β-NiAl precipitates) (Ref. 21). However, the driving force for precipitate growth also depends on the amount of supersaturation (Refs. 19, 20).

Calculated solubility plots of Cu in 17-4 and Al in 13-8+Mo can be seen in Fig. 8. Martensite could not be included in the calculations as it is a metastable phase. Thus, ferrite was considered instead. The changes in ferrite stability and solubility were expected to be like those of martensite due to the similarity between the two phases (Ref. 3). The plots include temperatures up to 750°C (1382°F) and 800°C (1472°F) for 13-8+Mo and 17-4, respectively, since ferrite was not stable above these temperatures. The nominal concentration of Cu and Al in their respective alloys are labeled on the plots. Note that the range of temperatures over which the Cu concentration in 17-4 exceeds the solubility limit was much larger than that of Al in 13-8+Mo. Therefore, even though the diffusion rate of Al in 13-8+Mo was higher than Cu in 17-4, the temperature range for precipitation and extent of supersaturation were significantly smaller in 13-8+Mo. Thus, there was decreased driving force for precipitate growth in 13-8+Mo when compared to 17-4, and a slower hardening response would thus be expected. Even though the precipitation response was not as significant in 13-8+Mo, both alloys showed an increase in hardness, which indicated the times and temperatures associated with welding thermal cycles were sufficient to promote hardening in the softened region of the HAZ.

Comparison of Base Metal and Weld Metal Hardening Response

The as-solidified weld metal microstructure for 17-4 and 13-8+Mo can be seen in Fig. 9. These alloys both solidify as δ-ferrite transform to austenite on cooling and, eventually, to martensite on further cooling (Refs. 1, 4, 22). The weld

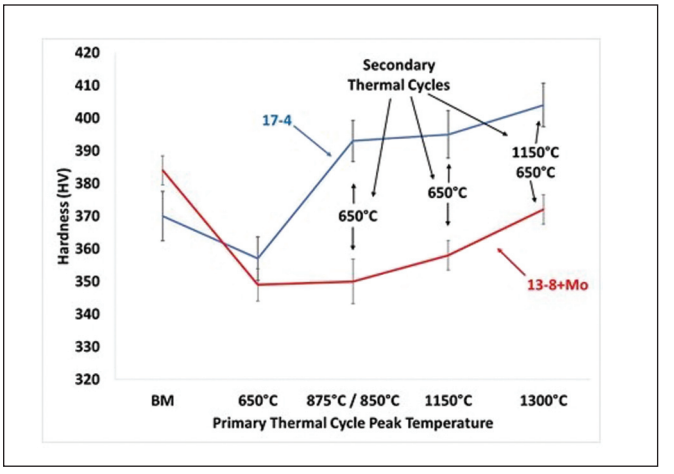

Fig. 7 — Hardness comparison for 1000 J/mm heat input between 17-4 and 13-8+Mo for the same secondary thermal cycle combinations.

metal exhibited a martensitic structure with remnant δ-ferrite. The 17-4 and 13-8+Mo weld metal samples were also subjected to the welding thermal cycle combinations listed in Table 2 for a 2000 J/mm and 1000 J/mm heat input, respectively. Hardness measurements were recorded before and after primary thermal cycles and the results are shown in Fig. 10. The as-welded material was significantly lower in hardness relative to the age-hardened base metal. The low hardness of the as-deposited weld metal was expected. After solidification, ferrite will transform to austenite, which has a relatively high solubility limit for the precipitating elements. Reduced solubility and concomitant precipitation require the formation of martensite. However, the transformation to martensite occurs below 200°C (392°F) where diffusion is slow and precipitation is unlikely to occur (Refs. 4, 23). After primary and secondary thermal cycles, the weld metal demonstrated a similar increase in hardness as its respective base metal for each material. A direct comparison between weld metal and base metal for 17-4 can be seen in Fig. 11, as an example. The hardness in 17-4 returned to near base metal levels or greater and the hardness in 13-8+Mo approached that of the base metal. Fusion zones of-

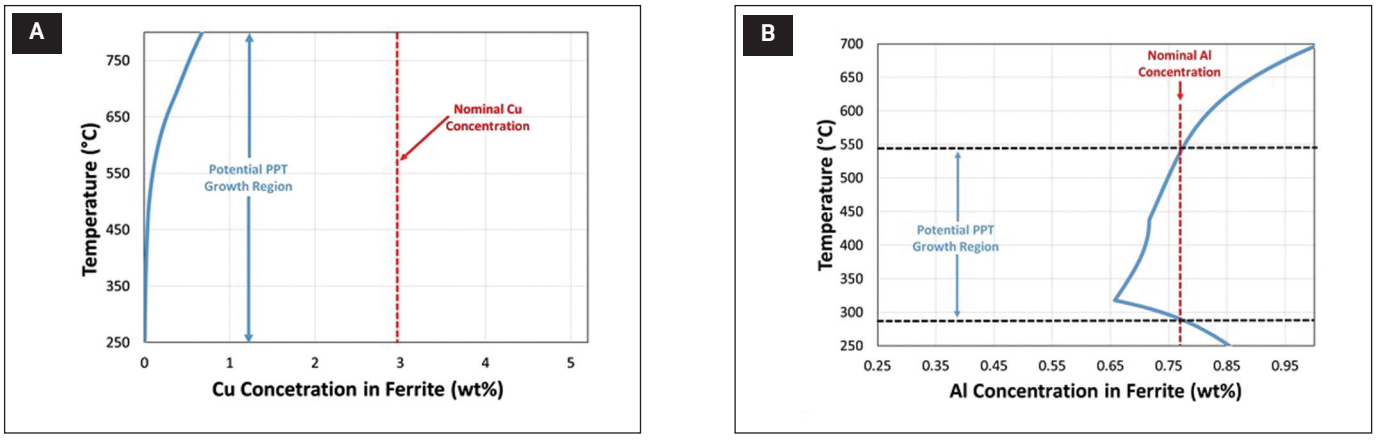

Fig. 8 — Calculated solubility limits of the following: A — Cu in ferrite for 17-4; B — Al in ferrite for 13-8+Mo.

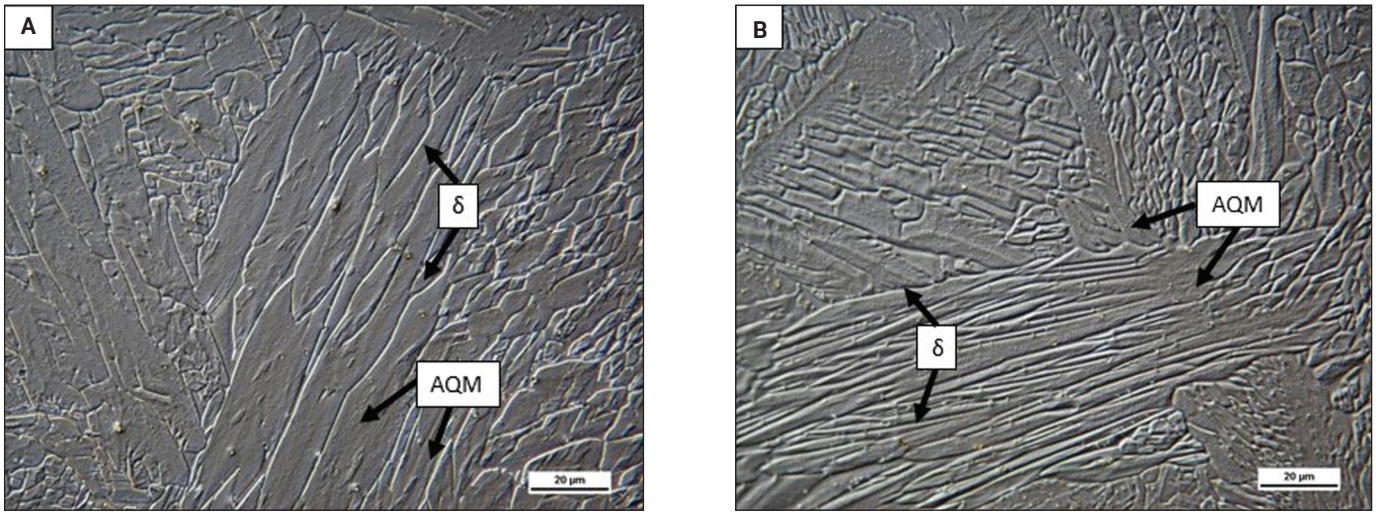

Fig. 9 — Weld metal microstructure of the following: A — 17-4; B — 13-8+Mo prior to Gleeble simulation. AQM = as-quenched martensite, δ = δ-ferrite.

ten exhibit remnant microsegregation that can inhibit precipitation in the solute-depleted cell/dendrite cores that solidify first (Ref. 24). However, the similarity in precipitation response between the base metal and weld metal suggests that the concentration of the precipitating solute elements in the weld metal is relatively uniform for each alloy.

Results from microchemical measurements acquired across the dendritic substructure for 17-4 and 13-8+Mo can be seen in Fig. 12. In general, the results indicated the Cr and Al concentrations were higher and the Ni and Cu concentrations were lower in ferrite regions when compared to the martensite. These results were expected since Cr and Al are ferrite stabilizers while Ni and Cu are known to stabilize austenite (and the austenite will subsequently transform to martensite on cooling) (Ref. 3). It is also evident that the Cu in 17-4 and Al in 13-8+Mo showed minimal variation within the martensitic regions. This is significant because the martensitic regions contain the high dislocation density necessary for precipitate formation and strengthening (Refs. 8, 25). The relatively uniform concentration profile for the major precipitating elements in each system accounted for the similar precipitation response observed in the weld metal and base metal. These results are in good agreement with the findings of Brooks and Garrison (Ref. 1) who measured the extent of segregation in the weld metal of three maraging stainless steels including 13-8+Mo. In their work, the dendrite core and boundary concentration of Al only varied by 0.2 wt-% after solidification.

The lack of compositional variation in the weld metal martensite indicated that either limited segregation occurred between the solid and liquid during solidification, and/or that backdiffusion was active and relieved any concentration gradients that may have formed. To assess this in more detail, Scheil nonequilibrium solidification calculations were performed. These calculations assume no liquid undercooling, complete diffusion in the liquid, no diffusion in the solid, and equilibrium at the solid/liquid interface. Thus, these calculations give an estimate of the maximum amount of segregation that could be expected. Additionally, equilibrium solidification calculations were performed to determine the minimum amount of segregation that could occur. The relationships for the Scheil and Equilibrium calculations can be seen in Equations 1 and 2, respectively (Ref. 26)

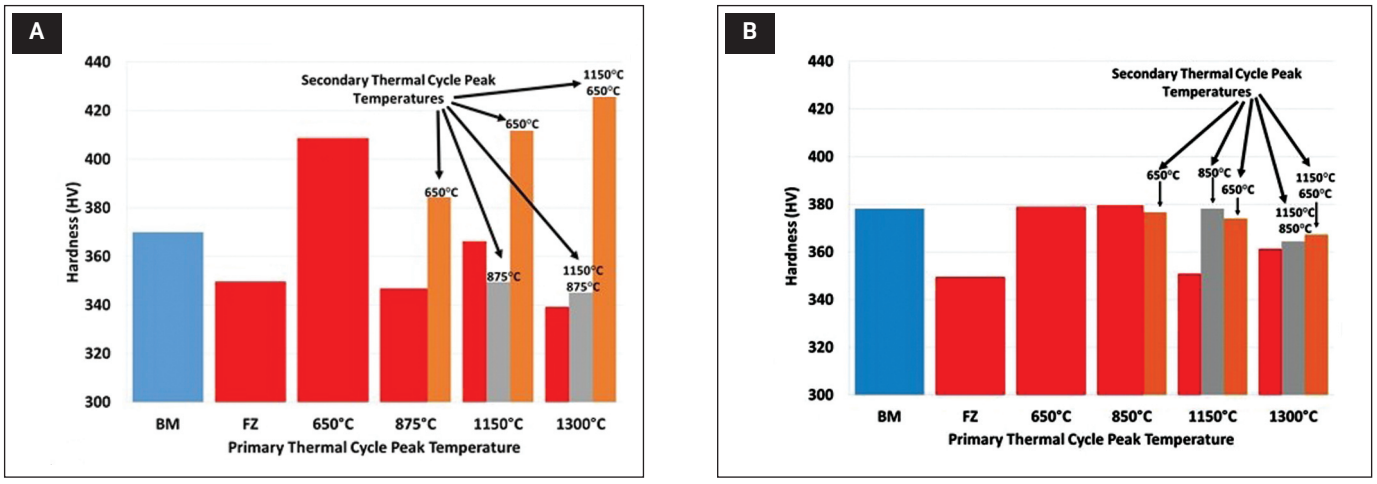

Fig. 10 — Hardness data for Gleeble multipass welding simulations. Red represents the as-welded fusion zone and fusion zone after primary thermal cycles. Orange and gray correlate to secondary thermal cycles. Blue is the age-hardened base metal. A — 17-4; B — 13-8+Mo.

$$kC_o(1-f_s)^{k-1} \quad (1)$$

$$\frac{kC_o}{f_s(k-1)+1} \quad (2)$$

where k is the partitioning coefficient, C_0 is the nominal solute concentration, and f_s is the fraction solid. Calculations were also performed to determine if the segregation that occurs due to solute redistribution between the solid and liquid during solidification could be relieved by backdiffusion. Backdiffusion during solidification can be estimated using the following equations developed originally by Brody and Flemings (Ref. 27) and later refined by Clyne and Kurz (Ref. 28).

$$C_s^* = kC_0\left[1-(1-2\alpha' k)f_s\right]^{\frac{k-1}{1-2\alpha' k}} \quad (3A)$$

$$f_s = \left(\frac{1}{1-2\alpha' k}\right)\left[1-\left(\frac{T_m-T}{T_m-T_l}\right)^{\frac{1-2\alpha' k}{k-1}}\right] \quad (3B)$$

$$\alpha' = \alpha\left[1-\exp\left(-\frac{1}{\alpha}\right)\right]-\frac{1}{2}\exp\left(-\frac{1}{2\alpha}\right) \quad (3C)$$

$$\alpha = \frac{D_s t_f}{L^2} \quad (3D)$$

where C_s^* is the solute concentration at the solid/liquid interface at a given fraction solid after backdiffusion, k is the partitioning coefficient, C_0 is the nominal solute concentration, f_s is the fraction solid, T_m is the melting point of the pure solvent, T_l is the liquidus temperature of the alloy, D_s is the diffusivity of the solute in body centered cubic (BCC) Fe, t_f is the solidification time, and L is half the dendrite arm spacing. The partition coefficient is the ratio of the solute concentration in the solid and liquid at a given temperature. An average value of k was calculated using concentrations from the ThermoCalc Scheil simulation as 0.56 for Cu in 17-4 and 1.15 for Al in 13-8+Mo. SmartWeld was used to estimate the fusion zone thermal cycle for each alloy for a 2000 J/mm heat input. The solidification time was then estimated from each thermal cycle as the time between the solidification start and finish temperatures calculated by ThermoCalc. Times of 0.44 s and 0.31 s were determined for 17-4 and 13-8+Mo, respectively. Half of the dendrite arm spacing was measured on average to be approximately 9 µm for both alloys.

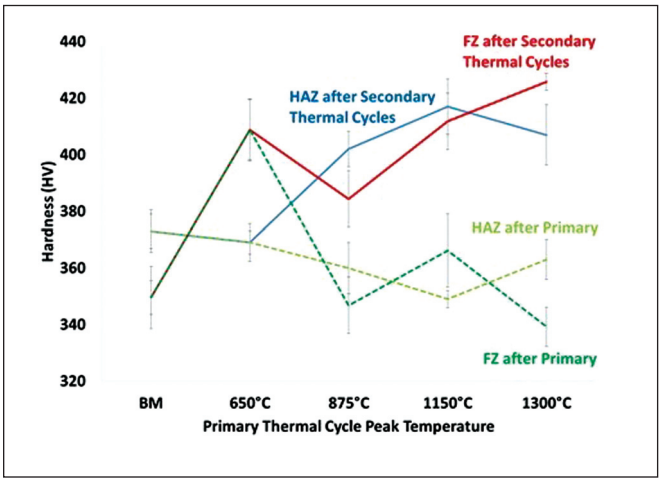

Fig. 11 — Comparison of the base metal and fusion zone hardness for 17-4 after exposure to the same secondary thermal cycle combinations.

The diffusion rates will vary significantly as temperature changes during solidification. Thus, diffusion rates of Cu and Al in BCC Fe were taken from literature for temperatures just below the liquidus and just above the solidus for each alloy to bound the calculations (Ref. 29). The results are shown in Fig. 13, and are accompanied by the Scheil and equilibrium concentration profiles for each alloy. From Fig. 8A, the solubility of Cu in ferrite was about 0.7 wt-% (at~775°C (1427°F)) and decreased with decreasing temperature. This value was shown

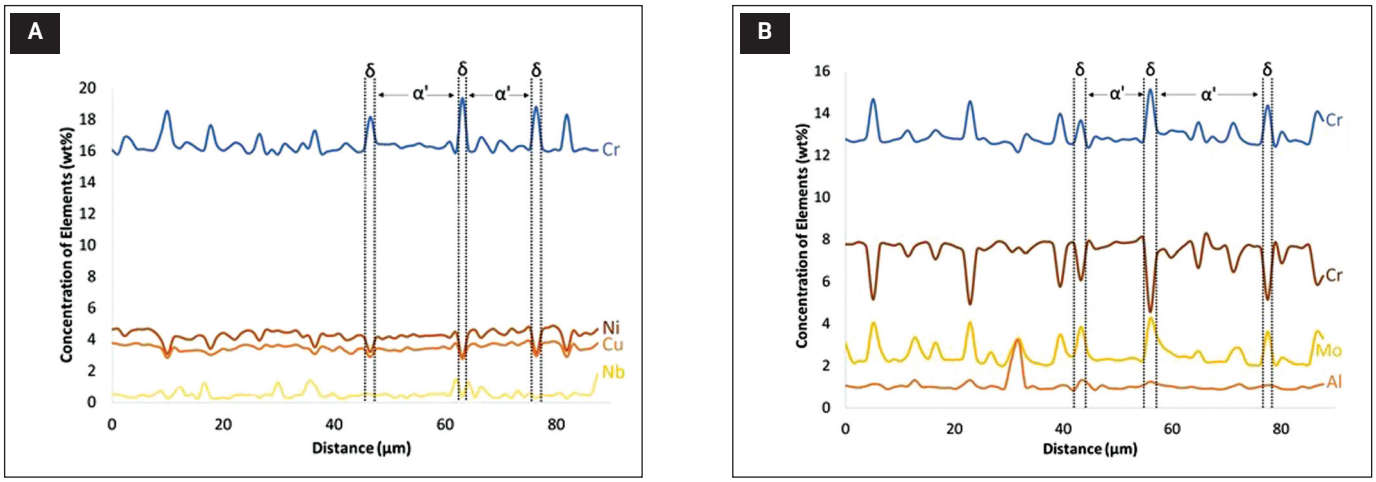

Fig. 12 — Concentration of select elements measured across multiple dendrites in the as-deposited weld metal samples for the following: A — 17-4; B — 13-8+Mo.

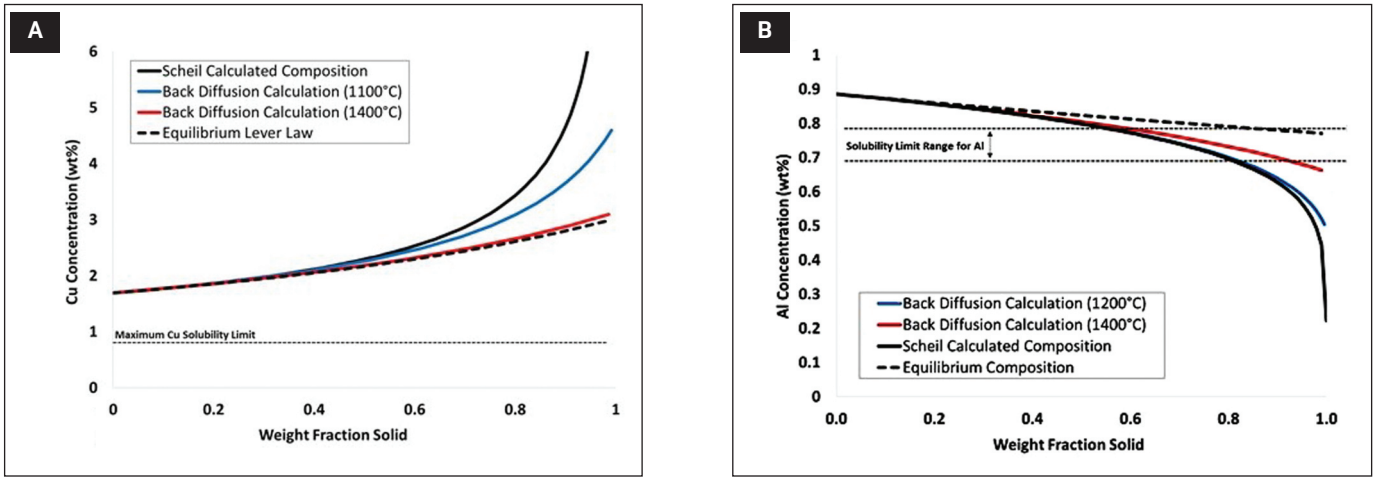

Fig. 13 — Estimated backdiffusion per Equation 3A for the following: A — Cu in 17-4; B — Al in 13-8+Mo.

for reference on Fig. 13A. Under nonequilibrium conditions (i.e., most extensive segregation), the Cu concentration in 17-4 was expected to always exceed the solubility limit of the ferrite indicating supersaturation would exist over all regions of the dendritic substructure. From Fig. 8B, the solubility range of Al in ferrite was about 0.66 to 0.77 wt-% (from ~ 285°C (545°F) to 550°C (1022°F)), and this range is shown in Fig. 13B. For nonequilibrium solidification conditions, the Al concentration could be as low as 0.22 wt-% in 13-8+Mo, indicating there would be regions within the dendritic substructure of Alloy 13-8+Mo where supersaturation would not exist and precipitation could therefore not occur. However, the backdiffusion calculations demonstrated that significant diffusion is expected during solidification for both 17-4 and 13-8+Mo. The Al concentration increases in the interdendritic regions to as high as 0.66 wt-% in 13-8+Mo. Additionally, the Cu concentration gradient in 17-4 demonstrated significant reduction. These results, when taken together with the measured concentration profiles, demonstrated that the concentration of Cu and Al in the weld metal of these alloys is relatively uniform, and this accounts for the similarity in precipitation response between the base metal and weld metal samples.

Conclusions

Samples of 17-4 and 13-8+Mo were subjected to primary and secondary thermal cycles representative of multipass welding. Thermal cycles for a 1000 and 2000 J/mm heat input were used on aged-hardened material and weld metal. Hardness testing was performed to estimate the extent of precipitate growth and dissolution. The following conclusions can be drawn from this work.

1. The temperatures experienced during primary welding thermal cycles result in precipitate dissolution and a concurrent decrease in hardness in 17-4 and 13-8+Mo.

2. Secondary thermal cycles resulted in an increase in hardness for each alloy indicating re-precipitation was occurring. The longer times associated with the 2000 J/mm heat input resulted in a greater increase in hardness than the lower heat input by allowing more time for precipitation to occur.

3. The hardening response of the weld metal is similar to the base metal for each alloy, which was attributed to backdiffusion that produced relatively uniform concentrations of

the precipitating elements in each system.

4. Cu precipitation in 17-4 occurs more rapidly than β-NiAl in 13-8+Mo and was attributed to more supersaturation and a wider temperature range over which supersaturation is present and precipitation can occur.

Acknowledgments

The authors gratefully acknowledge financial support for this work from the AMC Casting Solutions for Readiness program that is sponsored by the Defense Supply Center, Philadelphia, Pa., and the Defense Logistics Agency Research & Development (R&D) Office, Ft. Belvoir, Va.

References

1. Brooks, J. A., and Garrison Jr., W. M. 1999. Weld microstructure development and properties of precipitation-strengthened martensitic stainless steels. *Welding Journal* 78(8): 280-s to 291-s.

2. Bhaduri, A. K., and Venkadesan, S. 1989. Microstructure of the heat-affected zone in 17-4 PH stainless steel. *Steel Research* 60 (11): 509–513. DOI: 10.1002/srin.198901694

3. Bhadeshia, H., and Honeycombe, R. 2011. *Steels: Microstructure and Properties*. pp. 183 to 208. Oxford, UK: Butterworth-Heinemann. DOI: 10.1016/B978-0-7506-8084-4.X5000-6

4. Lippold, J. C., and Kotecki, D. J. 2005. *Welding Metallurgy and Weldability of Stainless Steels*. pp. 264 to 285. Hoboken, N.J.: Wiley.

5. Gladman, T. 1999. Precipitation hardening in metals. *Material Science and Technology* 15(1): 30–36. DOI: 10.1179/026708399773002782

6. Guo, Z., and Sha, W. 2002. Quantification of precipitation hardening and evolution of precipitates. *Materials Transactions* 43(6): 1273–1282. DOI: 10.2320/matertrans.43.1273

7. Hamlin, R. J., and DuPont, J. N. 2017. Microstructural evolution and mechanical properties of simulated heat-affected zones in cast precipitation-hardened stainless steels 17-4 and 13-8+Mo. *Metallurgical and Materials Transactions A* 48(1): 246–264. DOI: 10.1007/s11661-016-3851-6

8. Hochanadel, P. W., Edwards, G. R., Robino, C. V., and Cieslak, M. J. 1994. Heat treatment of investment cast PH 13-8 Mo stainless steel: Part I. Mechanical properties and microstructure. *Metallurgical and Materials Transactions A* 25(4): 789–798. DOI: 10.1007/BF02665455

9. Viswanathan, U. K., Banerjee, S., and Krishnan, R. 1988. Effects of aging on the microstructure of 17-4 PH stainless steel. *Materials Science and Engineering: A* 104: 181–189. DOI: 10.1016/0025-5416(88)90420-X

10. Bhaduri, A. K., Sujith, S., Srinivasan, G., Gill, T. P. S., and Mannan, S. L. 1995. Optimized postweld heat treatment procedures for 17-4 PH stainless steels. *Welding Journal* 74(5): 153-s to 159-s.

11. Yu, X., Caron, J. L., Babu, S. S., Lippold, J. C., Isheim, D., and Seidman, D. N. 2011 Strength recovery in a high-strength steel during multiple weld thermal simulations. *Metallurgical and Materials Transactions A* 42(12): 3669–3679. DOI: 10.1007/s11661-011-0707-y

12. Fuerschbach, P. W., and Eisler, G. R. 2002. Determination of material properties for welding models by means of arc weld experiments. *Sixth Int. Conf. Trends in Welding Research*. pp. 15–19. Phoenix, Ariz.

13. Fuerschbach, P. W., Eisler, G. R., and Steele, R. J. 1998. *Weld procedure development with OSLW-optimization software for laser welding*. pp. 1–4, Albuquerque, N.Mex., Sandia National Labs.

14. Reed, R. C., and Bhadeshia, H. K. D. H. 1994. A simple model for multipass steel welds. *Acta Metallurgica et Materialia* 42(11): 3663–3678. DOI: 10.1016/0956-7151(94)90432-4

15. Andersson, J. O., Helander, T., Höglund, L., Shi, P., and Sundman, B. 2002. Thermo-Calc & DICTRA, computational tools for materials science. *Calphad* 26(2): 273–312. DOI: 10.1016/S0364-5916(02)00037-8

16. Kou, S. 2003. *Welding Metallurgy*. pp. 449–453. Hoboken, N.J.: Wiley. DOI: 10.1002/0471434027

17. Ping, D. H., Ohnuma, M., Hirakawa, Y., Kadoya, Y., and Hono, K. 2005. Microstructural evolution in 13Cr–8Ni–2.5Mo–2Al martensitic precipitation-hardened stainless steel. *Materials Science and Engineering: A* 394(1-2): 285–295. DOI: 10.1016/j.msea.2004.12.002

18. Bono, J. T., DuPont, J. N., Jain, D., Baik, S. I., and Seidman, D. N. 2015. Investigation of strength recovery in welds of NUCu-140 steel through multipass welding and isothermal post-weld heat treatments. *Metallurgical and Materials Transactions A* 46(11): 5158–5170. DOI: 10.1007/s11661-015-3087-x

19. Porter, D. A., and Easterling, K. E. 1992. *Phase Transformations in Metals and Alloys, Third Edition*. pp. 265–295. London and New York: CRC Press.

20. Christian, J. W. 2002. *The Theory of Transformations in Metals and Alloys*. pp. 718–796. Oxford, UK: Pergamon. DOI: 10.1016/S1369-7021(03)00335-3

21. Brandes, E. A., and Brook, G. B. 1992. *Smithells Metals Reference Book, Seventh Edition*. pp. 13-1 to 13-118. Oxford, UK: Butterworth-Heinemann. DOI: 10.1016/C2009-0-25363-3

22. Cieslak, M. J., Hills, C. R., Hlava, P. F., and David, S. A. 1990. An investigation of the high-temperature and solidification microstructures of PH 13-8 Mo stainless steel. *Metallurgical Transactions: A* 21(9): 2465–2475. DOI: 10.1007/BF02646991

23. Robino, C. V., Cieslak, M. J., Hochanadel, P. W., and Edwards, G. R. 1994. Heat treatment of investment cast PH 13-8 Mo stainless steel: Part II. Isothermal aging kinetics. *Metallurgical and Materials Transactions A* 25(4): 697–704. DOI: 10.1007/BF02665446

24. DuPont, J. N., Lippold, J. C., and Kiser, S. D. 2011. *Welding Metallurgy and Weldability of Nickel-Base Alloys*. pp. 57–80. Hoboken, N.J.: Wiley. DOI: 10.1002/9780470500262

25. Viswanathan, U. K., Nayar, P. K. K., and Krishnan R. 1989. Kinetics of precipitation in 17–4 PH stainless steel. *Materials Science and Technology*. 5(4): 346–349. DOI: 10.1179/mst.1989. 5.4.346

26. DuPont, J. N., Marder, A. R., Notis, M. R., and Robino, C. V. 1998. Solidification of Nb-bearing superalloys: Part II. Pseudoternary solidification surfaces. *Metallurgical and Materials Transactions A* 29(11): 2797–2806. DOI: 10.1007/s11661-998-0320-x

27. Bower, T. F., Brody, H. D., and Flemings, M. C. 1966. Measurements of solute redistribution in dendritic solidification. *Transactions of the Metallurgical Society of AIME* 236: 624–633.

28. Clyne, T. W., and Kurz, W. 1981. Solute redistribution during solidification with rapid solid state diffusion. *Metallurgical Transactions: A* 12(6): 965–971. DOI: 10.1007/BF02643477

29. Oikawa, H. 1982. Review on lattice diffusion of substitutional impurities in iron. *Technology Reports of Tohoku University* 47(2): 215–224.

ROBERT J. HAMLIN (roberthamlin184@gmail.com) *and JOHN N. DuPONT are with the Department of Materials Science and Engineering, Lehigh University, Bethlehem, Pa.*